Open access • Journal Article • DOI:10.1117/1.JATIS.3.2.025001

Speckle statistics in adaptive optics images at visible wavelengths — Source link

Marco Stangalini, Fernando Pedichini, Enrico Pinna, Julian C. Christou ...+10 more authors

Institutions: Astronomical Observatory of Rome, Arcetri Astrophysical Observatory, University of Arizona, Stanford University ...+1 more institutions

Published on: 25 Apr 2017 - Journal of Astronomical Telescopes, Instruments, and Systems (SPIE)

Topics: Speckle pattern, Speckle noise, Speckle imaging and Adaptive optics

Speckle statistics in adaptive optics images at visible wavelengths

Journal of Astronomical Telescopes, Instruments, and Systems

AstronomicalTelescopes.SPIEDigitalLibrary.org

Speckle statistics in adaptive optics images at visible wavelengths

Marco Stangalini
Fernando Pedichini
Enrico Pinna
Julian Christou
John Hill
Alfio Puglisi
Vanessa Bailey
Mauro Centrone
Dario Del Moro
Simone Esposito
Fabrizio Fiore
Emanuele Giallongo
Phil Hinz
Amali Vaz

SPIE.

Marco Stangalini, Fernando Pedichini, Enrico Pinna, Julian Christou, John Hill, Alfio Puglisi, Vanessa Bailey, Mauro Centrone, Dario Del Moro, Simone Esposito, Fabrizio Fiore, Emanuele Giallongo, Phil Hinz, Amali Vaz, "Speckle statistics in adaptive optics images at visible wavelengths," *J. Astron. Telesc. Instrum. Syst.* **3**(2), 025001 (2017), doi: 10.1117/1.JATIS.3.2.025001.

Speckle statistics in adaptive optics images at visible wavelengths

Marco Stangalini,[a,b,*] Fernando Pedichini,[a,b] Enrico Pinna,[b,c] Julian Christou,[d] John Hill,[d] Alfio Puglisi,[b,c] Vanessa Bailey,[e] Mauro Centrone,[a] Dario Del Moro,[f] Simone Esposito,[b,c] Fabrizio Fiore,[a,b] Emanuele Giallongo,[a,b] Phil Hinz,[g] and Amali Vaz[g]

[a]INAF-OAR, Astronomical Observatory of Rome, National Institute for Astrophysics, Monte Porzio Catone, Italy
[b]ADONI Adaptive Optics National Lab of Italy, Italy
[c]INAF-Arcetri Astrophysical Observatory of Florence, National Institute for Astrophysics, Florence, Italy
[d]University of Arizona, LBTO, Tucson, Arizona United States
[e]KIPAC-Stanford University, Stanford, California, United States
[f]Universitá di Roma Tor Vergata, Rome, Italy
[g]University of Arizona, CAAO, Steward Observatory, Tucson, Arizona, United States

Abstract. Residual speckles in adaptive optics (AO) images represent a well-known limitation on the achievement of the contrast needed for faint source detection. Speckles in AO imagery can be the result of either residual atmospheric aberrations, not corrected by the AO, or slowly evolving aberrations induced by the optical system. We take advantage of the high temporal cadence (1 ms) of the data acquired by the System for Coronagraphy with High-order Adaptive Optics from R to K bands-VIS forerunner experiment at the Large Binocular Telescope to characterize the AO residual speckles at visible wavelengths. An accurate knowledge of the speckle pattern and its dynamics is of paramount importance for the application of methods aimed at their mitigation. By means of both an automatic identification software and information theory, we study the main statistical properties of AO residuals and their dynamics. We therefore provide a speckle characterization that can be incorporated into numerical simulations to increase their realism and to optimize the performances of both real-time and postprocessing techniques aimed at the reduction of the speckle noise. [DOI: 10.1117/1.JATIS.3.2.025001]

Keywords: adaptive optics; atmospheric optics; speckle phenomena.

Paper 16052P received Oct. 14, 2016; accepted for publication Apr. 10, 2017; published online Apr. 25, 2017.

1 Introduction

Speckle noise represents one of the major limitations on the detection of faint companions to nearby stars.[1] Although current high contrast imaging instruments and coronagraphs make use of sophisticated and high performance AO systems,[2] small optical imperfections yield quasistatic speckles and residual stray light, which still represents a severe limitation on achieving the high contrast needed to detect faint companions.[3–6] For these reasons, a deep understanding of the speckle variability and statistics is of fundamental importance for the optimization of postfacto techniques aimed at increasing the image contrast,[7–9] such as angular differential imaging (ADI), locally optimized combination of images, and principal component analysis.[10–13] In addition, it has been demonstrated that speckle intensity statistics represents a powerful tool for speckle discrimination and, therefore, for their postfacto suppression.[14] To detect an Earth-like planet at a close angular distance from a bright star, a flux contrast of the order of 10^{-10} is required. Unfortunately, a final (after postprocessing) contrast larger than $\sim 10^{-6}$ cannot be currently expected even in AO-assisted coronagraphic systems operated under the best seeing conditions at short-wave infrared wavelengths.[8] Furthermore, an accurate knowledge of the speckle pattern and its dynamics is crucial for increasing the realism of simulations aimed at optimizing the instrument performance.

The analysis of the dynamic behavior of AO residuals can be used to estimate the decorrelation time of the atmospheric turbulence and thus its predictability horizon. In Ref. 6, it was recently shown that one of the major limitations on the achievement of the very high contrast needed in exoplanet imaging is represented by the servo-lag error in the extreme adaptive optics (ExAO) systems. Indeed, even a short time lag of 1 or 2 ms can result in a large decrease of the bandwidth of the system and, thus, of the overall performances and contrast. In Ref. 15 and, more recently, in Ref. 16, it has been demonstrated that over timescales consistent with the frozen flow approximation, the wavefront aberrations are predictable. In particular, in Ref. 16, it was shown that 20% to 40% of the power spectral density of wavefront fluctuations is due to frozen flow. To mitigate the effects of the servo-lag error, several authors have proposed AO control schemes based on different forecasting approaches. See for instance Refs. 17–19. Very recently, the validity of this approach was demonstrated on sky.[20] The study of the dynamics of AO residuals and their decorrelation time is also useful for investigating the limits of the applicability of such techniques.

Several authors have already investigated the statistical properties of speckles in AO corrected images.[21–24] However, these statistical studies have mostly focused on intensity fluctuations in specific locations of the focal plane, using data sequences with a limited temporal cadence (>40 to 50 ms), longer than the typical atmospheric timescales (5 to 10 ms). Recently,

*Address all correspondence to: Marco Stangalini, E-mail: marco.stangalini@inaf.it

2329-4124/2017/$25.00 © 2017 SPIE

other authors[9] have investigated the speckle lifetime in the H-band by exploiting a 1.6-Hz cadence set of ExAO images.

To complement these studies, in this work, we exploit new data acquired by the System for Coronagraphy with High-order Adaptive Optics from R to K bands (SHARK) forerunner experiment[25–28] at a very high cadence (1 ms) and visible wavelengths. These data allow us to study the behavior of residual AO speckles down to very short timescales and assess the atmospheric clearance time with very high accuracy. In addition, we exploit these data to study the spatial distribution of long-lived speckles, which, as already mentioned, represent a severe limitation on the achievement of very high contrast in ADI images.

2 Data Set

The data set used in this work consists of a series of 1-ms exposure images of the target Gliese 777 (1-ms cadence), acquired with the SHARK forerunner experiment at Large Binocular Telescope (LBT) on June 4, 2015 [see Fig. 2(a)]. The pixel scale was set at 3.73 mas, and the imager was a Zyla CMOS camera manufactured by Andor Inc. The total duration of the data series is 20 min (or equivalently 1,200,000 images). During the acquisition, the LBT Interferometer (LBTI)-AO system[29] was correcting 500 modes in closed loop. The AO frequency was 1 KHz with a loop delay of 3 ms. In this condition, the closed loop 0-db bandwidth was 59 Hz. The seeing S was in the range of $0.8 < S < 1.5$ arcsec, and no field derotator was employed on the mount to correct for the sky rotation.

The SHARK-VIS forerunner experiment was a set of short test observations performed at the LBT telescope to verify its AO system performance at visible wavelengths ($600 < \lambda < 900$ nm) between February and June 2015.[28] The experimental setup was minimal and composed of only two optical elements before the detector: a divergent lens to get a super sampling (twice the Nyquist limit) of the PSF (point spread function) and a 40-nm FWHM filter centered at 630 nm. The AO control and wavefront sensing were left to the LBTI adaptive optics (AO) subsystem fed through a 50% beam splitter. All the forerunner hardware was placed on a steel optical breadboard for easy customization and attached to the LBT main structure. Data acquisition was performed using an in-house developed LabView software interfacing the Andor Zyla sCMOS (Scientific CMOS) camera with a camera link to a PCI board yielding a maximum throughput of 140 Mpixel/s digitized at 16 bit. The short exposure time (1 ms) was used to freeze the evolution of atmospheric speckles and to easily recover the residual jitter in the focal plane, for its postfacto correction. We remark here that residual jitter in longer exposure images may affect the results of the statistical analysis of residual speckles. Our very fast cadence allows us to reduce this effect by employing a postfacto registration of the data sequence. Our target was acquired at low zenith angles to avoid PSF elongation due to atmospheric differential refraction and close to the meridian to maximize the effect of field rotation, which is useful for ADI postprocessing of image stacks.

The data calibration process consists of the dark frame subtraction and image registration through a fast Fourier transform (FFT) phase correlation technique. In short, the FFT cross-correlation between the two images was computed, and the phase was estimated from it. For two perfectly matching images, the cross-phase is a function with a peak at the center of the image domain. When one of the two images is shifted with respect to the other, the position of the peak of the phase function is shifted by an amount of pixels corresponding to the exact shift between the two images themselves. By fitting a Gaussian to the phase function, it is possible to estimate the shift (i.e., the position of its peak) with subpixel accuracy.

In Fig. 1(a), we show an image of the target obtained by adding up to 1,200,000 unsaturated images after their subpixel registration. This is equivalent to a 20-min exposure time. In Fig. 1(b), we also show a radial profile of the same long-exposure PSF. In this work, we focus our attention on both regions within and outside the radius at which the AO system is effectively suppressing the atmospheric aberrations. This corresponds to a distance from the optical axis, which is commonly referred to as control radius,[30] and depends on the number of actuators of the deformable mirror (DM), the wavelength, and telescope diameter. The control radius is represented by the dashed line in Fig. 1. At larger radial distances, the DM is not able to suppress aberration modes, and the PSF is dominated by seeing.

The speckles within the control radius are those that are due to either AO residual aberrations or quasistatic distortions due, for example, to noncommon path aberrations (NCPA). Hereafter, we refer to these speckles as "AO residuals," while we refer to the speckles outside the control radius as "seeing-induced speckles." However, it is worth mentioning here that the SHARK forerunner is designed to minimize NCPA

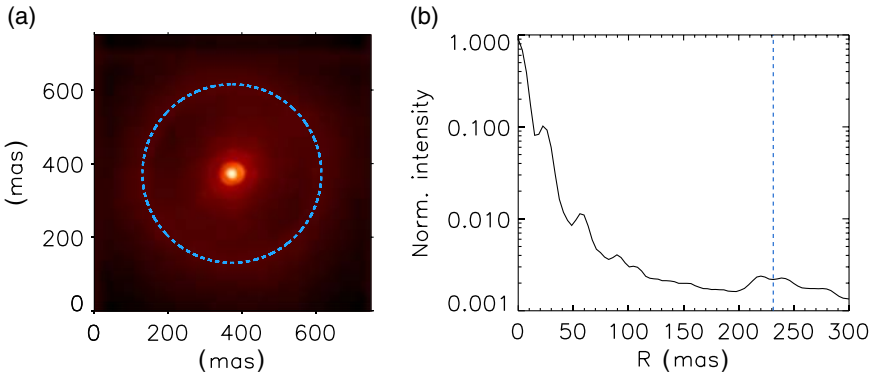

Fig. 1 (a) Sum of 1,200,000 coregistered images (20-s equivalent long exposure) of Gliese 777 in logarithmic scale. The dashed circle indicates the approximate position of the control radius. (b) Normalized radial profile of the long exposure image. The vertical dashed line indicates the control radius.

aberrations by simplifying its optical path and picking the beam off very close to the wavefront sensor.[25,27] Further, during the observation, the NCPAs aberrations were mitigated by injecting an offset on the secondary DM of LBT following the procedure described in Ref. 31.

3 Methods and Results

3.1 *Speckle Lifetime Statistics*

To estimate the lifetime of the two populations of speckles within and outside the control radius (i.e., AO residuals and seeing-induced, respectively), speckles are identified and tracked using the SWAMIS tracking code.[32] This code was originally written for the identification and tracking of small-scale magnetic elements in the solar photosphere;[33–35] a task conceptually similar to that of the analysis of AO residual faint speckles in SHARK forerunner data.[36,37] In short, the code identifies and tracks, through sequential images, small-scale features that are above a user-specified threshold (4σ in our case), where σ is the standard deviation of the signal (intensity) computed in a dark region in the upper left corner of the image and covering at least an area of n pixels (where $n = 16$ in our case). This implies that only structures with a size of the order of the PSF are identified and tracked, thus ruling out the possibility of including noise features. For a speckle to be uniquely identified, these two thresholds have to be met at the same time.

With the aim of reducing the computational time, instead of using the entire set of images (1,200,000), we limit ourselves to the analysis of different temporal windows of 5 s (5000 images) during the observation run. Indeed, even if looking at this short interval, the number of speckles identified and matching the above criteria amounts to about 90,000. This is a large number, ensuring a good estimation of the underlying statistics.

Here, we focus our attention on the first temporal window at the beginning of the data sequence, while at the end of this section we will extend the analysis to the other temporal windows.

After the identification of the speckles matching the searching criteria, the code assigns a label to each of them. This label is unique throughout the data series and permits the identification of the speckles at different time steps. In Fig. 2(b), we show an example of masks obtained from the identification of the speckles in the images shown in Fig. 2(a). In the same panels, we also show the labels of each speckle, which represent its unique identifier during its entire life.

To distinguish possible differences between the two populations of speckles, we separate them into two classes: those lying within the control radius and those outside (see blue dashed line in Fig. 1), and for each of them, we measure the lifetime and the maximum intensity throughout their entire life.

It is worth noting that the selection criteria described above do not allow the code to single out speckles in proximity to the center of the PSF [see Fig. 2(b)]. Despite this, a large amount of speckles are identified within the control radius anyway, thus ensuring the statistical significance of the results.

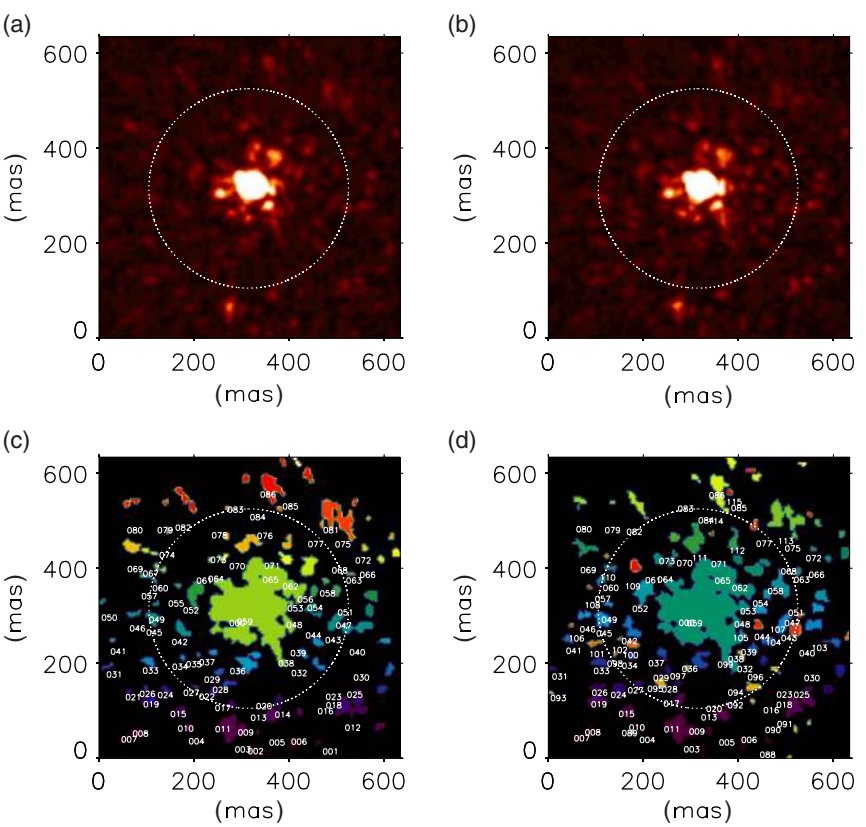

Fig. 2 (a) Two sample logarithmically scaled images, sequentially acquired every one millisecond and (b) identification of speckles through the SWAMIS code. The speckles are labeled with different colors. Each speckle is assigned a unique identifier throughout the whole data sequence. The white circles indicate the position of the control radius. Only speckles within this radius are considered in the analysis (see text for more details).

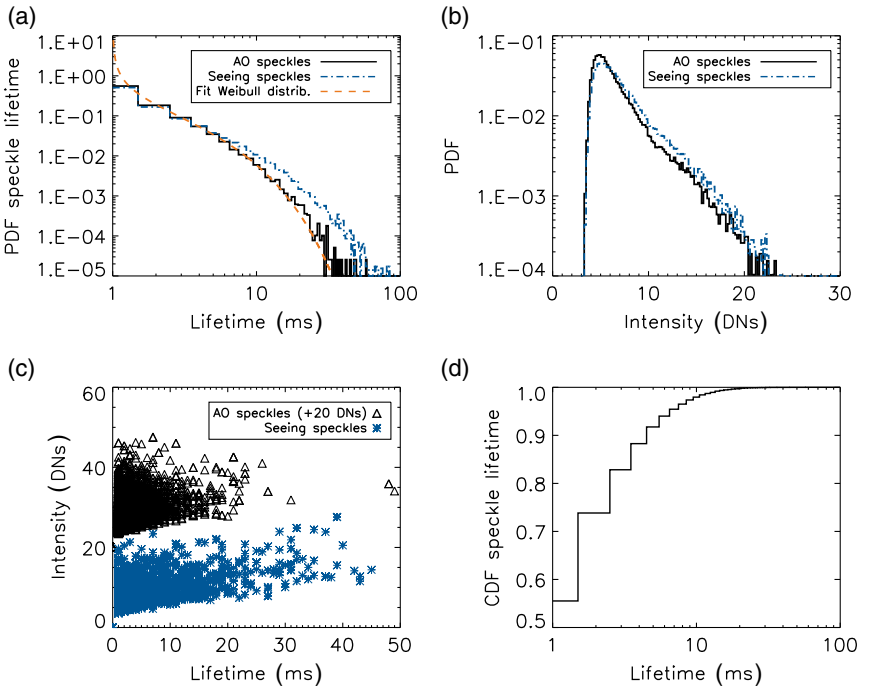

Fig. 3 (a) PDF of the lifetimes of the AO and seeing speckles. The orange line represents the least squares fit to the data of a Weibull distribution. (b) PDF of the intensity of both populations of speckles. (c) Lifetime-intensity relation for the two samples. Please note that the intensity of the AO residual speckles was shifted upward by an amount equivalent to 10 DNs for graphical reasons. (d) CDF of the AO speckle lifetime.

In Fig. 3(a), we show the probability density function (PDF) of lifetimes for the two samples of speckles. As one can note from the same figure, the PDF can be modeled by a two-parameter Weibull distribution[38] of the form

$$f(t) = \frac{\beta}{\eta}\left(\frac{t}{\eta}\right)^{(\beta-1)} \exp\left(-\frac{t}{\eta}\right)^{\beta}, \quad (1)$$

where t is the time, β is a shape parameter, and η is a scaling parameter, also known as characteristic time. The least squares fit to the data yields $\beta = 0.25$ and $\eta = 1$ ms. It is worth recalling that, by definition, the η time scale of the Weibull distribution represents the time at which ~63.2% of the sampled population die.

Apart from the physical meaning (Weibull distributions are usually found in turbulence as the signature of random multiplicative processes[39]), this represents a simple form that can be easily incorporated into numerical simulations of high contrast coronagraphic imagers to improve the accuracy of their estimated contrast.

It is worth noting that the PDF of the lifetimes of seeing-induced speckles, as compared to that of the AO residuals, shows a larger density of elements in the range of 20 to 70 ms, if compared to the PDF of the AO residuals. This is in agreement with previous results in the literature showing that the AO system only modifies the intensity of speckles, leaving their lifetime unchanged.[4] Indeed, this effect can be due to the intensity threshold used for the identification of the speckles. In Fig. 3(b), we show that the PDF of the intensity of the seeing-induced speckles presents an intrinsically larger amount of elements, with respect to the intensity distribution of AO residuals, in the bright end. In the presence of an almost linear dependence of the lifetime on the intensity [see Fig. 3(c)], this translates into an increase in the probability of detection of long-lived speckles outside the control radius of the PSF. Brighter speckles remain above the selection threshold longer than the fainter ones, resulting in an increase in the fraction of the identified longest-lived speckles themselves. However, except for this increase, the two PDFs do not show significant differences.

Another important aspect by far is the estimation of the atmospheric refreshing time, which is the time over which the speckle pattern is completely renewed.

Regarding this, in Fig. 3(b), we show the cumulative distribution function (CDF) of the AO speckle lifetime. The CDF represents the probability of finding a speckle with a lifetime τ_{spk} shorter than τ. The CDF shows that while 50% of the speckles

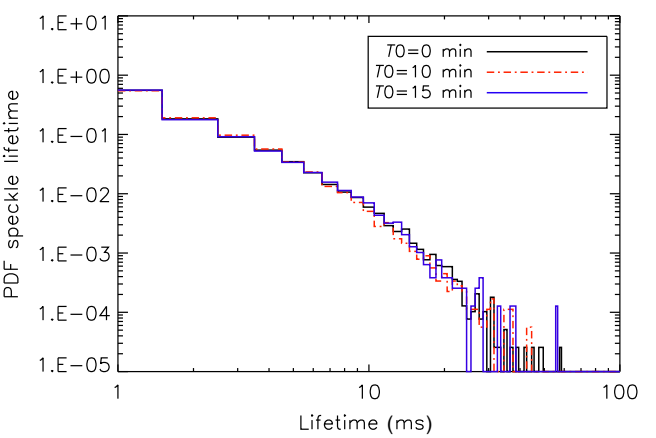

Fig. 4 PDF of the AO speckles lifetime computed in different temporal windows (6 s each) along the entire data sequence.

identified have a lifetime of the order of 1 ms, 99% of them are found within 20 ms. This means that, after this time, the speckle pattern is almost completely renewed, and this value can be considered as the refreshing time scale of the atmospheric turbulence.

The above results were obtained by analyzing a temporal window of 5 s at the beginning of the data sequence ($T_0 = 0$ min). To be sure that the statistics does not depend on the particular temporal window selected, as already mentioned, we repeated the analysis over different temporal windows (i.e., $T_0 = 0$, $T_0 = 10$ min, and $T_0 = 15$ min). The results of this analysis are shown in Fig. 4. where we plot the PDFs of the speckle lifetime for each temporal window selected. This plot shows that the PDF of lifetimes does not change significantly during the observation.

3.2 *Mutual Information and Memory of the Process*

To independently check the above results, we make use of a completely different approach based upon information theory.[40] More particularly, we make use of the mutual information (MI),[41,42] which is a measure of the nonlinear mutual dependence of two variables X and Y, and is defined as

$$\mathrm{MI}(X,Y) = \sum_{y\epsilon Y}\sum_{x\epsilon X} p(x,y)\,\log\left[\frac{p(x,y)}{p(x)p(y)}\right], \tag{2}$$

where $p(x,y)$ represents the joint probability function and $p(x)$ and $p(y)$ are the PDFs of X and Y, respectively. It is a well-known result that, while the correlation is a measure of the linear dependence between two variables, MI is a more general quantity that can also be applied to nonlinear processes.[43] MI was already employed in the AO field, in the optimization of the wavefront reconstruction.[44]

Since the statistics of speckles does not change during the observation, here, we focus on the first temporal window analyzed at the beginning of Sec. 3.1. We divided the first 5 s of the observations into short subsequences of 100 ms each. This is possible since in 100 ms the speckle pattern is completely refreshed. For each subsequence, we estimated the MI between the first and any other following image. This is done by only considering the region of the field of view within the control radius, which is marked by the dashed blue line of Fig. 1. In Fig. 5, we plot the average MI as a function of the delay τ. We stress here that this analysis is only made possible by the high cadence of the data. As expected, MI undergoes a rapid decrease as the time delay goes by. This indicates a rapid decrease of correlation of the process with time. After ~20 ms, MI reaches an asymptotic value, indicating the presence of a persistent pattern of residues. Most of the speckles have a very short lifetime (shorter than 20 ms), and, consequently, the MI drops by almost 80% in 1 ms (MI = 1 for $\tau = 0$ by definition). The rapid reduction of MI reflects the short memory of the process associated with the evolution of the atmospheric turbulence, which determines a fast evolution of the speckle pattern. Indeed, after 20 ms, the speckle pattern is completely renewed, and the mutual dependence between the current and the first PSFs is reduced to a minimum. However, it is worth noting that the asymptotic value of the MI is not zero, as expected for statistically independent images. As already anticipated, this implies that there exists a quasistatic component of the pattern itself. However, this component accounts for only ~6% of the total information contained in the speckle images. We note that the estimated value of the decorrelation time obtained through MI is in good agreement with that estimated by the PDF of the lifetimes seen in Sec. 3.1.

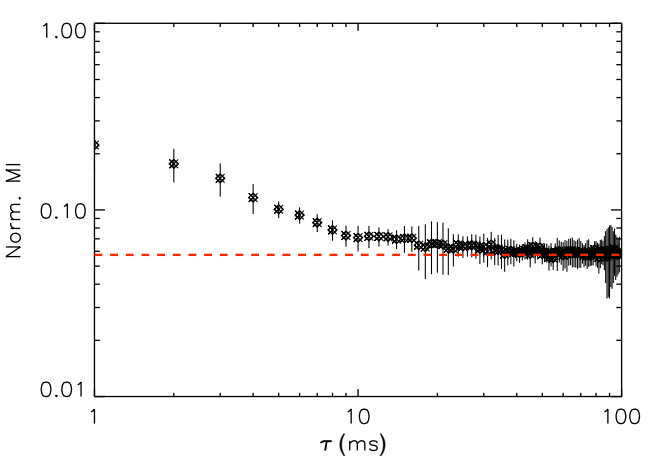

Fig. 5 MI as a function of the time delay. The error bars represent the standard error of the mean of the 50 sequences of 100 ms over which the MI is computed. The MI is estimated for each image with respect to the beginning of the sequence. The horizontal dashed line represents the asymptotic value of the MI estimated as the average value between 80 and 100 ms.

It is interesting to note that the error bars in the plot, representing the standard errors of the mean of the 50 sequences, oscillate in size reflecting the intrinsic spread of the MI estimated from the different sequences.

3.3 *Spatial Distribution of Quasistatic Speckles*

To further investigate the nature of AO residual speckles, we also analyze their spatial distribution by estimating the FFT spatial spectra of intensity fluctuations. More particularly, we focus our attention on the spatial distribution of the longest-lived components of the intensity fluctuations with the aim of investigating the character of quasistatic speckles. If images are averaged over a sufficiently longer time (say 7 to 10 times the clearance time), we expect to significantly reduce the contribution from seeing-induced and rapidly disappearing speckles, with only the ones commonly referred to as quasistatic speckles left in the images. To study the spatial contribution of this latter component, we average our entire data sequence (20-min duration) in windows of 200 ms to get rid of the rapidly evolving speckle component. For each of these "long exposure" images, we estimate the spatial FFT spectrum after masking out pixels outside the control radius, over which the DM has no effect. The masking is performed with a gently decreasing function without sharp edges to avoid side effects in the FFTs $[1 - H(x,y)$, where $H(x,y)$ represents the Hanning window centered at the PSF peak]. We then consider the average amplitude spectrum of the spatial fluctuations as our best estimate of the quasistatic speckles spatial distribution in the Fourier space. The spatial spectrum of the fluctuations due to quasistatic speckles can be modeled as follows:[45]

$$P(F_s) = \frac{A_0}{[1 + (F_s/A_1)]^{\frac{A_2+1}{2}}}, \tag{3}$$

where F_s represents the spatial frequency.

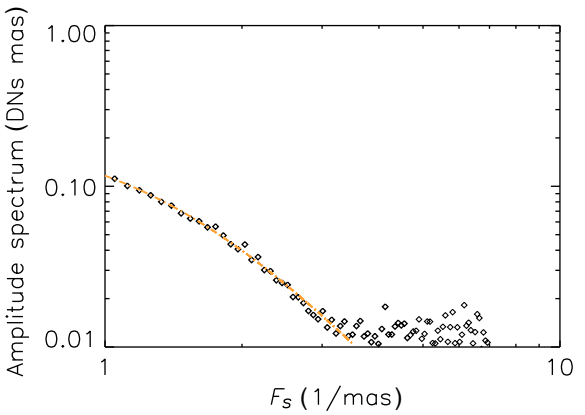

Fig. 6 FFT amplitude spectrum of the quasistatic speckles as a function of the spatial frequency F_s. The dashed line represents the fit of the Terrestrial Planet Finder model to the data points.

In Fig. 6, we show the mean amplitude of the spatial spectrum of residual speckles. A least squares fit of the above model to the data in the range of 1 to 3 mas^{-1} yields the following estimates for the three parameters: $A_0 = 0.2 \pm 0.04$ DNs $\cdot$ mas, $A1 = 1.40 \pm 0.05$ mas^{-1}, and $A_2 = 2.0 \pm 0.2$.

4 Concluding Remarks

Our results show that the turbulence clearance time at visible wavelength is of the order of 20 ms. Indeed, 99.9% of the statistical sample of speckles detected in our data have a lifetime shorter than this value. The CDF of the speckles lifetime shows that those with a lifetime longer than ~70 ms are very few, only 0.15 speckle/s. In addition, the PDF of the lifetime of the AO residual speckles is found to be well represented by a Weibull distribution. This is not surprising since this distribution is generally used to model lifetimes of different physical processes in a wide range of contexts.[38] However, it is worth stressing here that the accurate modeling of the PDF of lifetimes is only made possible by the high frame rate of the SHARK-VIS forerunner experiment that, delivering images with a cadence of 1 ms, freezes the atmospheric turbulence evolution. The clearance time of the atmospheric turbulence is estimated in this work through two different approaches (automatic speckle identification and information theory) from closed-loop AO images and can be regarded as a decorrelation time scale of the spatial pattern of speckles. After this time, the speckle pattern is completely regenerated.

Our results demonstrate that, at least in these particular observing conditions, the decorrelation time of the atmospheric aberrations is much longer than the AO correction frequency (1 kHz). It is worth noting here that 90% of the speckles have a lifetime shorter than 5 ms; thus, the overall predictability horizon of the wavefront aberrations must lie in this range. In other words, at visible wavelengths, most of the memory of the system is already lost after 5 ms, thus setting an intrinsic limit on the predictability of the process, which is much shorter than the decorrelation time. This is important for the implementation of AO predictive control schemes in the visible.

In addition to this, we also estimated the spatial distribution of the quasistatic speckles, after averaging out the seeing-induced ones. The power spectrum of the quasistatic speckles is well represented by the model proposed in Ref. 45. However, in this work, we are able to provide an accurate estimate of their parameters due to the high cadence of our data.

This piece of information is important for increasing the realism of end-to-end AO simulations for the assessment of the performances of high contrast imagers in real on-sky conditions.

It is worth noting that our characterization of the speckle statistics is based on a particular set of observing conditions. However, we also note that this is the first time that seeing-induced residual speckles are characterized down to time scales as small as 1 ms. This is due to the high acquisition cadence of the SHARK forerunner that allowed us to perform a detailed characterization of the dynamics of the speckles themselves.

Acknowledgments

The LBT is an international collaboration among institutions in the United States, Italy, and Germany. LBT Corporation partners are: Istituto Nazionale di Astrofisica, Italy; The University of Arizona on behalf of the Arizona Board of Regents; LBT Beteiligungsgesellschaft, Germany, representing the Max-Planck Society, The Leibniz Institute for Astrophysics Potsdam, and Heidelberg University; The Ohio State University, and The Research Corporation, on behalf of The University of Notre Dame, University of Minnesota, and University of Virginia. This work was partially funded by the Adaptive Optics National Laboratory of Italy, and by the European Commission's H2020 project GREST, grant Agreement No. 653982.

References

1. R. Racine et al., "Speckle noise and the detection of faint companions," *PASP* **111**, 587–594 (1999).
2. E. Hugot et al., "Active optics methods for exoplanet direct imaging-stress polishing of supersmooth aspherics for VLT-sphere planet finder," *A&A* **538**, A139 (2012).
3. C. Marois et al., "Efficient speckle noise attenuation in faint companion imaging," *Publ. Astron. Soc. Pac.* **112**(767), 91–96 (2000).
4. B. Macintosh et al., "Speckle lifetimes in high-contrast adaptive optics," *Proc. SPIE* **5903**, 59030J (2005).
5. C. Cavarroc et al., "Fundamental limitations on earth-like planet detection with extremely large telescopes," *A&A* **447**(1), 397–403 (2006).
6. M. Kasper, "Adaptive optics for high contrast imaging," *Proc. SPIE* **8447**, 84470B (2012).
7. P. Martinez et al., "Speckle temporal stability in XAO coronagraphic images," *A&A* **541**, A136 (2012).
8. P. Martinez et al., "Speckle temporal stability in XAO coronagraphic images. II. Refine model for quasi-static speckle temporal evolution for VLT/SPHERE," *A&A* **554**, A41 (2013).
9. J. Milli et al., "Speckle lifetime in XAO coronagraphic images: temporal evolution of sphere coronagraphic images," *Proc. SPIE* **9909**, 99094Z (2016).
10. C. Marois et al., "Angular differential imaging: a powerful high-contrast imaging technique," *Astrophys. J.* **641**, 556–564 (2006).
11. D. Lafrenière et al., "A new algorithm for point-spread function subtraction in high-contrast imaging: a demonstration with angular differential imaging," *Astrophys. J.* **660**, 770–780 (2007).
12. R. Soummer, L. Pueyo, and J. Larkin, "Detection and characterization of exoplanets and disks using projections on Karhunen–Loève eigenimages," *Astrophys. J.* **755**, L28 (2012).
13. A. Amara and S. P. Quanz, "PYNPOINT: an image processing package for finding exoplanets," *Mon. Not. R. Astron. Soc.* **427**, 948–955 (2012).
14. S. Gladysz, N. Yaitskova, and J. C. Christou, "Statistics of intensity in adaptive-optics images and their usefulness for detection and photometry of exoplanets," *J. Opt. Soc. Am. A* **27**, A64–A75 (2010).
15. M. B. Jorgenson and G. J. M. Aitken, "Prediction of atmospherically induced wave-front degradations," *Opt. Lett.* **17**, 466–468 (1992).
16. L. Poyneer, M. van Dam, and J.-P. Véran, "Experimental verification of the frozen flow atmospheric turbulence assumption with use of astronomical adaptive optics telemetry," *J. Opt. Soc. Am. A* **26**, 833 (2009).

17. N. J. Doelman et al., "Optimal control strategy to reduce the temporal wavefront error in AO systems," *Proc. SPIE* **5490**, 1426–1437 (2004).
18. M. Stangalini et al., "Multiple field-of-view MCAO for a large solar telescope: LOST simulations," *Proc. SPIE* **7736**, 77364H (2010).
19. K. Jackson et al., "Linear prediction of atmospheric wave-fronts for tomographic adaptive optics systems: modelling and robustness assessment," *Opt. Lett.* **40**, 143 (2015).
20. J. Tesch et al., "On-sky demonstration of optimal control for adaptive optics at palomar observatory," *Opt. Lett.* **40**(7), 1575–1578 (2015).
21. C. Aime and R. Soummer, "The usefulness and limits of coronagraphy in the presence of pinned speckles," *Appl. J. Lett.* **612**, L85–L88 (2004).
22. C. Aime and R. Soummer, "The effect of a coronagraph on the statistics of adaptive optics pinned speckles," in *EAS Publications Series*, C. Aime and R. Soummer, Eds., Vol. **12**, pp. 89–101, EDP Sciences (2004).
23. M. P. Fitzgerald and J. R. Graham, "Speckle statistics in adaptively corrected images," *Astrophys. J.* **637**, 541–547 (2006).
24. N. Yaitskova and S. Gladysz, "First-order speckle statistics for arbitrary aberration strength," *J. Opt. Soc. Am. A* **28**, 1909–1919 (2011).
25. M. Stangalini et al., "The solar system at 10 parsec: exploiting the ExAO of LBT in the visual wavelengths," *Proc. SPIE* **9147**, 91478F (2014).
26. J. Farinato et al., "SHARK (system for coronagraphy with high order adaptive optics from R to K band): a proposal for the LBT 2nd generation instrumentation," *Proc. SPIE* **9147**, 91477J (2014).
27. J. Farinato et al., "The NIR arm of SHARK: system for coronagraphy with high-order adaptive optics from R to K bands," *Int. J. Astrobiol.* **14**, 365–373 (2015).
28. F. Pedichini et al., "High contrast imaging in the visible: first experimental results at the Large Binocular Telescope," ArXiv e-prints (2016).
29. S. Esposito et al., "First light AO (FLAO) system for LBT: final integration, acceptance test in Europe, and preliminary on-sky commissioning results," *Proc. SPIE* **7736**, 773609 (2010).
30. R. Davies and M. Kasper, "Adaptive optics for astronomy," *Ann. Rev. Astron. Astrophys.* **50**, 305–351 (2012).
31. S. Esposito et al., "Non common path aberration correction with non linear WFSS," in *Adaptive Optics for Extremely Large Telescopes 4–Conf. Proc.*, Vol. 1 (2015).
32. C. E. DeForest et al., "Solar magnetic tracking. I. software comparison and recommended practices," *Astrophys. J.* **666**, 576–587 (2007).
33. D. A. Lamb et al., "Solar magnetic tracking. II. The apparent unipolar origin of quiet-sun flux," *Astrophys. J.* **674**, 520–529 (2008).
34. D. A. Lamb et al., "Solar magnetic tracking. III. Apparent unipolar flux emergence in high-resolution observations," *Astrophys. J.* **720**, 1405–1416 (2010).
35. D. A. Lamb et al., "Solar magnetic tracking. IV. The death of magnetic features," *Astrophys. J.* **774**, 127 (2013).
36. M. Stangalini, "Photospheric supergranular flows and magnetic flux emergence," *A&A* **561**, L6 (2014).
37. M. Stangalini, F. Giannattasio, and S. Jafarzadeh, "Non-linear propagation of kink waves to the solar chromosphere," *A&A* **577**, A17 (2015).
38. W. Weibull, "A statistical distribution function of wide applicability," *J. Appl. Mech.* **18**(3), 293–297 (1951).
39. U. Frisch and D. Sornette, "Extreme deviations and applications," *J. Phys.* **7**(9), 1155–1171 (1997).
40. C. E. Shannon, "A mathematical theory of communication," *ACM SIGMOBILE Mob. Comput. Commun. Rev.* **5**(1), 3–55 (2001).
41. L. Paninski, "Estimation of entropy and mutual information," *Neural Comput.* **15**(6), 1191–1253 (2003).
42. A. Kraskov, H. Stögbauer, and P. Grassberger, "Estimating mutual information," *Phys. Rev. E* **69**(6), 066138 (2004).
43. W. Li, "Mutual information functions versus correlation functions," *J. Stat. Phys.* **60**, 823–837 (1990).
44. M. Stangalini et al., "Zernike basis optimization for solar adaptive optics by using information theory," *Appl. Opt.* **49**(11), 2090–2094 (2010).
45. E. L. Church, P. Z. Takacs, and T. A. Leonard, "The prediction of BRDFS from surface profile measurements," *Proc. SPIE* **1165**, 136 (1990).

Marco Stangalini received his doctorate degree in astronomy at the University of Rome "Tor Vergata" in 2011. After that he became a postdoctoral research fellow at the Max Planck Institute for Solar Physics Research, Germany. He is now a researcher at the National Institute for Astrophysics (INAF) in Rome. His main research fields are MHD waves in the solar atmosphere and adaptive optics for high precision polarimetry.

Biographies of the other authors are not available.